OBSERVATION OF TeV GAMMA RAYS FROM THE CRAB NEBULA USING THE ATMOSPHERIC CERENKOV IMAGING TECHNIQUE

T. C. WEEKES,[1] M. F. CAWLEY,[2] D. J. FEGAN,[3] K. G. GIBBS,[1] A. M. HILLAS,[4] P. W. KWOK,[1] R. C. LAMB,[5]
D. A. LEWIS,[5] D. MACOMB,[5] N. A. PORTER,[3] P. T. REYNOLDS,[1,3] AND G. VACANTI[5]

ABSTRACT

The Whipple Observatory 10 m reflector, operating as a 37 pixel camera, has been used to observe the Crab Nebula in TeV gamma rays. By selecting gamma-ray images based on their predicted properties, more than 98% of the background is rejected; a detection is reported at the 9.0 σ level, corresponding to a flux of 1.8×10^{-11} photons cm^2 s^{-1} above 0.7 TeV (with a factor of 1.5 uncertainty in both flux and energy). Less than 25% of the observed flux is pulsed at the period of PSR 0531. There is no evidence for variability on time scales from months to years. Although continuum emission from the pulsar cannot be ruled out, it seems more likely that the observed flux comes from the hard Compton synchrotron spectrum of the nebula.

Subject headings: gamma rays: general — nebulae: Crab Nebula — pulsars — radiation mechanisms

I. INTRODUCTION

The observation of polarization in the radio, optical, and X-ray emission from the Crab Nebula is usually taken as confirmation of the synchrotron origin of the radiation and is a strong indication of the presence in the nebula of a reservoir of relativistic electrons with energies up to 1 TeV. The presence of the radio pulsar, PSR 0531, near the center of the nebula provides a source for the on-going injection of relativistic electrons into this reservoir. The collision of the synchrotron-radiating electrons with synchrotron-radiated photons within the nebula inevitably results in a hard photon spectrum (at some level) that extends from the X-ray into the gamma-ray energy range; the shape of the spectrum mirrors that of the soft photon spectrum but with greatly reduced intensity. The Compton synchrotron model of the nebula was first developed by Gould (1965) and was refined by Rieke and Weekes (1969) and by Grindlay and Hoffmann (1971). A strong flux of gamma rays was predicted with maximum luminosity in the 0.1–1.0 TeV energy range. The gamma-ray flux level depends on the strength of the nebular magnetic field, which is a free parameter in the model and is little constrained by observations at other wavelengths. However, based on equipartition arguments, it is estimated to be $\sim 10^{-3}$ G.

The observation of a flux of 0.14 TeV gamma rays from the Crab Nebula was reported by the Smithsonian group using the atmospheric Cerenkov technique (Fazio et al. 1972); based on observations that spanned 3 years, this detection was still only at the 3 σ level. This demonstrates both the weakness of the source and the lack of sensitivity of the technique. The detection of TeV gamma rays from the Crab Nebula is a confirmation of the Compton synchrotron model and gives a direct measure of the magnetic field. This measurement, which was conservatively interpreted as an upper limit, implies an average magnetic field of 3×10^{-4} G, or a radially symmetric $(1/r)$ field with $B_0 = 1 \times 10^{-3}$ G at a distance of 0.1 pc from the pulsar (Grindlay 1976).

Subsequent to the discovery of PSR 0531 in the nebula, TeV gamma-ray observations concentrated on the pulsar because greater sensitivity could be achieved by the assumption of synchronization of the gamma-ray emission with the periodic radio emission. Several detections were reported at very high energies (Grindlay 1972; Jennings et al. 1974; Grindlay, Helmken, and Weekes 1976; Porter et al. 1976; Erickson, Fickle, and Lamb 1976; Vishwanath 1982; Vishwanath et al. 1985; Gupta et al. 1977; Gibson et al. 1982b; Dowthwaite et al. 1984; Tumer et al. 1985; Bhat et al. 1986), but the statistical significance was not high, and upper limits were also presented which appeared to be in conflict with the reported fluxes (Helmken et al. 1973; Vishwanath et al. 1986; Bhat et al. 1987). At energies above 1 TeV there were also reports of emission from the direction of the Crab (Mukanov 1983; Boone et al. 1984; Dzikowski et al. 1981; Kirov et al. 1985), but, because of the limited angular resolution and the absence of accurate timekeeping, it was not possible to identify the source of the observed signal with the nebula or the pulsar. Again there may be conflicting upper limits (Craig et al. 1981; Watson 1985). At 100 MeV energies (which are accessible to study by spark chambers on satellites), both a pulsed and steady component were detected (Kniffen et al. 1977; Hermsen et al. 1977; Clear et al. 1987); at 1 GeV the strength of the unpulsed component (which might originate in the nebula or near the pulsar) is 0.25 times that of the pulsed flux.

Using a refined version of the atmospheric Cerenkov technique, we here report the detection of gamma rays above 0.7 TeV from the Crab Nebula at a high level of statistical significance; over the epoch 1986–1988 we find no evidence for variability, and the observed flux is in agreement with that reported previously in 1969–1972 and in an earlier observation utilizing this same technique in 1983–5 (Cawley et al. 1985a; Gibbs 1987). The observed gamma-ray flux is only 0.2% of the cosmic-ray background. A periodic analysis using the known radio period of the pulsar indicates that less than 25% of the observed signal is pulsed. The detection of such a weak flux from a steady (nonpulsed) source with a significance of 9 standard deviations (σ) is a milestone in the development of ground-based gamma-ray astronomy. It demonstrates the power of using atmospheric Cerenkov shower imaging to distinguish gamma-ray–initiated air showers from those gener-

[1] Harvard-Smithsonian Center for Astrophysics.
[2] St. Patrick's College, Maynooth.
[3] University College, Dublin.
[4] University of Leeds.
[5] Iowa State University.

ated by the much more numerous background of cosmic rays (Hill *et al.* 1963; Weekes and Turver 1977; Hillas 1985; Cawley *et al.* 1985*b*). With this technique there is little ambiguity about the nature of the primaries which produce the excess; these Cerenkov images are selected because they are photonic in character.

II. TECHNIQUE

a) Atmospheric Cerenkov Imaging

In its most rudimentary form (Porter and Weekes 1978), the atmospheric Cerenkov technique has provided telescopes for gamma-ray astronomy in the TeV energy region which have large collection areas (greater than 10^4 m^2) and high angular resolution ($<2°$). In these first generation systems the superficial similarity of the Cerenkov light from hadron- and gamma-ray–initiated air showers did not allow any differentiation between signal and background. Thus the gamma-ray flux sensitivity was limited severely, and most detections relied on the detection of a periodic signal for credibility.

However, a number of characteristics of the two kinds of showers (hadron- or gamma-ray–initiated) were suggested as possible discriminators, e.g., the presence of penetrating particles (Grindlay 1971), the ultraviolet excess (Stepanian, Fomin, and Vladimirsky 1983), the shape of the image (Hill *et al.* 1963; Hillas 1985), the time duration (Fegan *et al.* 1968; Resvanis *et al.* 1986). In addition, methods were developed for improving the angular resolution of the technique (Gibson *et al.* 1982*b*). To date, these developments have been only partially successful in improving the flux sensitivity relative to that achievable with first-generation detectors.

The atmospheric Cerenkov imaging technique offers the possibility of improved discrimination against background, as well as increased angular resolution with a single optical reflector. First suggested for image intensifiers coupled to small optical systems (Hill and Porter 1961), it achieved a more practical realization with the use of arrays of phototubes in the focal plane of large multifaceted optical reflectors (Weekes and Turver 1977; Weekes 1981; Zyskin *et al.* 1987).

b) 10 m Optical Reflector Camera

The Whipple Observatory 10 m optical reflector, located on Mount Hopkins in southern Arizona (elevation 2.3 km, latitude 31°5), is ideally suited for this purpose since it has excellent imaging properties and is at a dark location where there is a high percentage of clear skies. The instrument is dedicated to very high energy gamma-ray astronomy. The focal plane has a plate scale of 12.5 cm deg^{-1}. In 1983 it was converted into a fast 37 element camera for gamma-ray astronomy.

The 10 m optical reflector has a unique optical design. Its 248 hexagonal mirror facets each have a spherical figure with a 14.6 m radius of curvature and are individually mounted on a 7.3 m radius spherical support structure. Each facet then functions as an off-axis spherical mirror focusing light parallel to the optic axis of the reflector to the center of the 7.3 m sphere. Details of the design have been given elsewhere (Davies and Cotton 1957; Rieke 1969; Lewis *et al.* 1987). The point spread functions (intensity vs. position on the image surface for a point source at infinity) have been calculated and agree with measured values for both axial rays and rays 1°5 off the optic axis. In both cases, the full width at half maximum (FWHM) is $\sim 0°15$; the off-axis image has a small cometary tail which

points away from the center of the field of view. This shape does not arise from aberrations in the individual mirror facets as might be expected, but is a global effect resulting from the fact that the outer mirrors actually point in the wrong direction for off-axis incident rays. This does not change the FWHM but does diminish the concentration for off-axis images.

In the focal plane of the camera each picture element (pixel) consists of a RCA phototube (6342A/V1) with bialkali photocathode; each tube has a diameter of 5 cm (0°4), and the tubes are arranged in a hexagonal pattern with spacing of 6.25 cm (0°5) between pixel centers (Fig. 1). The full aperture of the camera is 3°5. We describe the camera in terms of zones. Zones 0, 1, 2, and 3 are, respectively, the inner tube, the ring of six, the ring of 12, and the outer ring of 18. Phototubes were chosen as detector elements because of the large plate scale and small f number which precludes the use of conventional imaging devices. The advantages of phototubes for this application are high quantum efficiency at blue wavelengths, low dark current/readout noise compared to the noise from the night-sky background, modularity, and high gain.

The output of each of the 37 phototubes was taken directly through 50 m of coaxial cable to the control room, where the signal was divided into its fast pulse and DC components. The fast pulse was taken to a fast amplifier (LeCroy 612) with dual outputs. One of these went, via 50 nsec of delay cable, to an analog-to-digital converter (ADC) (LeCroy 2249A with a gate width of 45 nsec and 10-bit resolution). For the inner 19 channels (the trigger channels), the second output went directly to a discriminator (LeCroy 623B) whose trigger level was set just above the intersection of the night-sky noise spectrum with the background shower pulse spectrum. The discriminator outputs went to a majority logic unit (MLU) (LeCroy 4532) set to trigger at the trigger levels greater than 1. This conservative trigger setting was chosen to give Cerenkov light images which might be usefully analyzed rather than operating at the lowest possible detector threshold. The resolving time was 10 nsec, limited primarily by the 6 nsec time spread inherent in the 10 m reflector optics. The MLU generated an event trigger which gated the ADCs and caused the readout of all 37 ADC channels, timing scalers, and an event type identifier. Each phototube had an adjustable high voltage power supply, allowing the gains to be preset to be approximately equal.

Timing pulses were also injected as event triggers at 1 minute intervals from a Rubidium clock, a WWVB radio receiver, and a sidereal clock; these timing pulses caused the interrogation of a multichannel scaler which monitored the trigger rates in each of the 19 trigger channels. The time of arrival of each event was recorded with an absolute time accuracy better than 0.5 msec and with a relative spacing known to 1 μsec.

The camera was CAMAC–controlled via a Digital Equipment Corporation LSI 11/73 computer; data were stored on hard disk and were transferred to magnetic tape at the end of each night of operation. During operation, the computer could be used to display individual events, the pulse height spectrum of each channel, the time history of the observation, etc.; data analysis was not performed on-line.

The current in each of the 19 trigger channels was servo-controlled with a padding lamp (LED) on the face of the phototube; this was to compensate for changes in the brightness of the star field seen by the phototube as the source (ON) or comparison (OFF) region was tracked. Typically these padding lamps were set to add 30% more current over that due
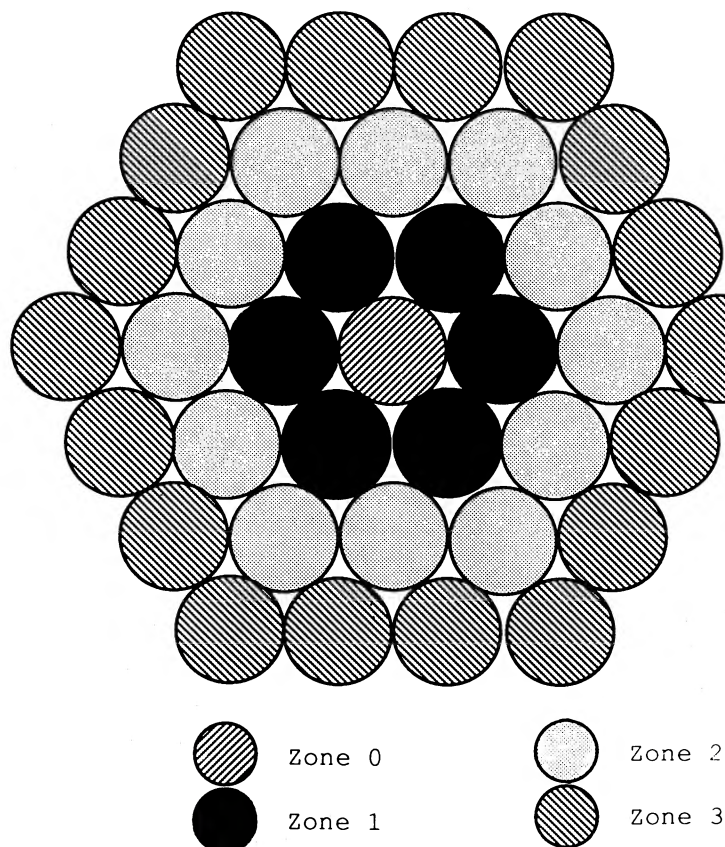
FIG. 1.—Layout of phototubes in the focal plane of the 10 m optical reflector. Each phototube has a sensitive area defined by a diameter of 0°4; the spacing between phototubes is 0°5. The full field of view is 3°5. The center phototube is defined as zone 0; the surrounding ring of six phototubes is zone 1, the ring of 12 zone 2, and the outer ring of 18 zone 3. The latter is not included in the camera trigger.

to the dark night sky. Although this system adds noise to each channel, it is considered essential if stable trigger conditions are to be maintained between the ON and OFF regions. Because the 10 m reflector is on an altazimuth mount, the star field slowly rotates as the source is tracked sidereally. The presence of a bright star ($m_v < +3.0$) in the field of view may exceed the padding lamp's ability to compensate for the changing light level in a particular phototube. If so, that phototube is turned off for the duration of the ON and OFF scans.

Typically the trigger rate in each channel was 1 Hz, and the event trigger rate was 3–4 Hz at the zenith. The latter had a zenith angle dependence that went as $R_z = R_0 \cos^{-2.5} z$, where R_0 is the rate at the zenith and z is the zenith angle. The random rate from night-sky fluctuations was negligible, but there was a small zenith-angle–dependent contribution to the trigger rate from cosmic-ray particles physically passing through two or more adjacent phototubes in the focus box. This rate was measured to be 0.01–0.03 Hz.

Noise limits the accuracy with which the shower image characteristics can be measured. There are three types of noise present in the recorded pulse heights: (1) shot noise in the signal itself; (2) noise due to fluctuations in the night-sky-light (plus padding lamp), which is also a form of shot noise; (3) pickup, electronic noise, etc., downstream of the phototubes. The latter was found to be negligible.

Under operating conditions (dark night sky) the average current in each phototube is 0.33 photoelectron per nsec. The night-sky noise is effectively the fluctuation in this number

within the 45 nsec integration time of the camera. Artificial triggers of the camera permitted this number to be measured; the result is ~5.9 photoelectrons per channel per gate width. The minimum possible is 3.9 photoelectrons, which is the Poisson standard deviation in the number of photoelectrons emitted by the photocathode. Thus we find a value 1.5 times the Poisson value.

Shot noise in the signal itself was measured by consideration of the fluctuations when the camera is triggered by a pulsed nitrogen discharge tube which uniformly illuminates each phototube (Lewis et al. 1987). These nitrogen flash images indicated that the measured signals show fluctuations that are 1.3 times the expected Poisson deviation, in approximate agreement with value derived above. These results are consistent with the expected noise due to the statistics of the dynode secondary emission process.

Absolute calibration of the camera is based upon consideration of the above noise levels and from a direct measurement using a calibrated radioactive light source on the face of each phototube. The light source was calibrated using an acrylic Cerenkov muon telescope (Gorham 1986). These measurements indicated a conversion factor of 1.4 photoelectrons per digital count. The trigger level for each of the 19 inner tubes was ~50 electrons.

c) Observations

The ON/OFF tracking technique was generally used for the observations of the Crab Nebula. The typical procedure was to

set the reflector to track the candidate source for 28 minutes; in this mode the source was within ±0°.1 of the optic axis throughout the ON scan. Then, in a 2 minute interval the reflector was slewed to point to a position 30 minutes later in right ascension and was allowed to track at the sidereal rate for 28 minutes during which the same range of zenith and azimuth angles were covered (OFF scan). This sequence of ON/OFF pairs was repeated as long as the sky conditions were excellent (no clouds) and the zenith angle z was less than 55°. The proximity of optical telescopes nearby meant that the observer was alerted to the presence of even very thin cirrus. The majority of the observations were taken at $z < 30°$.

For the observations of the Crab Nebula the presence of the star, Zeta Tau ($V = +3.0$, $B−V = −0.19$), $\sim 1°$ away from the source location on the sky, necessitated the removal of one phototube in zone 2 (by turning off its high voltage) per scan. The scan was timed to start so that the star would only fall in one phototube during the scan. During the corresponding OFF scan the same phototube was turned off.

Calibration files were recorded at the beginning and end of each night. These were (1) a "pedestal" file, in which the camera was triggered by a 10 Hz timing signal to record the pedestal levels of the ADCs; (2) a "sky pedestal" file, which was the same as (1) but had the high voltage turned on, so that the fluctuations due to the night-sky light were recorded; (3) a

"nitrogen" file in which the camera was triggered by a diffuse fast blue light (nitrogen spark) source located 8 m from the phototubes. In each case 500–1000 event triggers were recorded.

Additional information pertaining to routine operation was continuously recorded on video tape throughout the scans; this consisted of (1) tracking computer video output; (2) output of image-intensified camera view of sky ±3° around source; (3) video image of the padding lamps.

To confirm the quality of the camera operation on a nightly basis, a 15 minute observation was taken with the telescope pointed to the zenith at the beginning of each night. To ensure that the camera was operating efficiently before proceeding with the routine source observations, these data were analyzed using the on-line LSI-11 computer.

d) Image Processing

Preliminary data analysis consisted of three steps: (1) image normalization, calibration, and editing; (2) shower image parameterization; (3) candidate gamma-ray event selection. These selected images could then be used to look for an excess from the source direction or to search for periodicities in the data. In Figure 2 we show a typical image at various stages in the preparation process as well as the shower image parameters (defined below) derived from it.
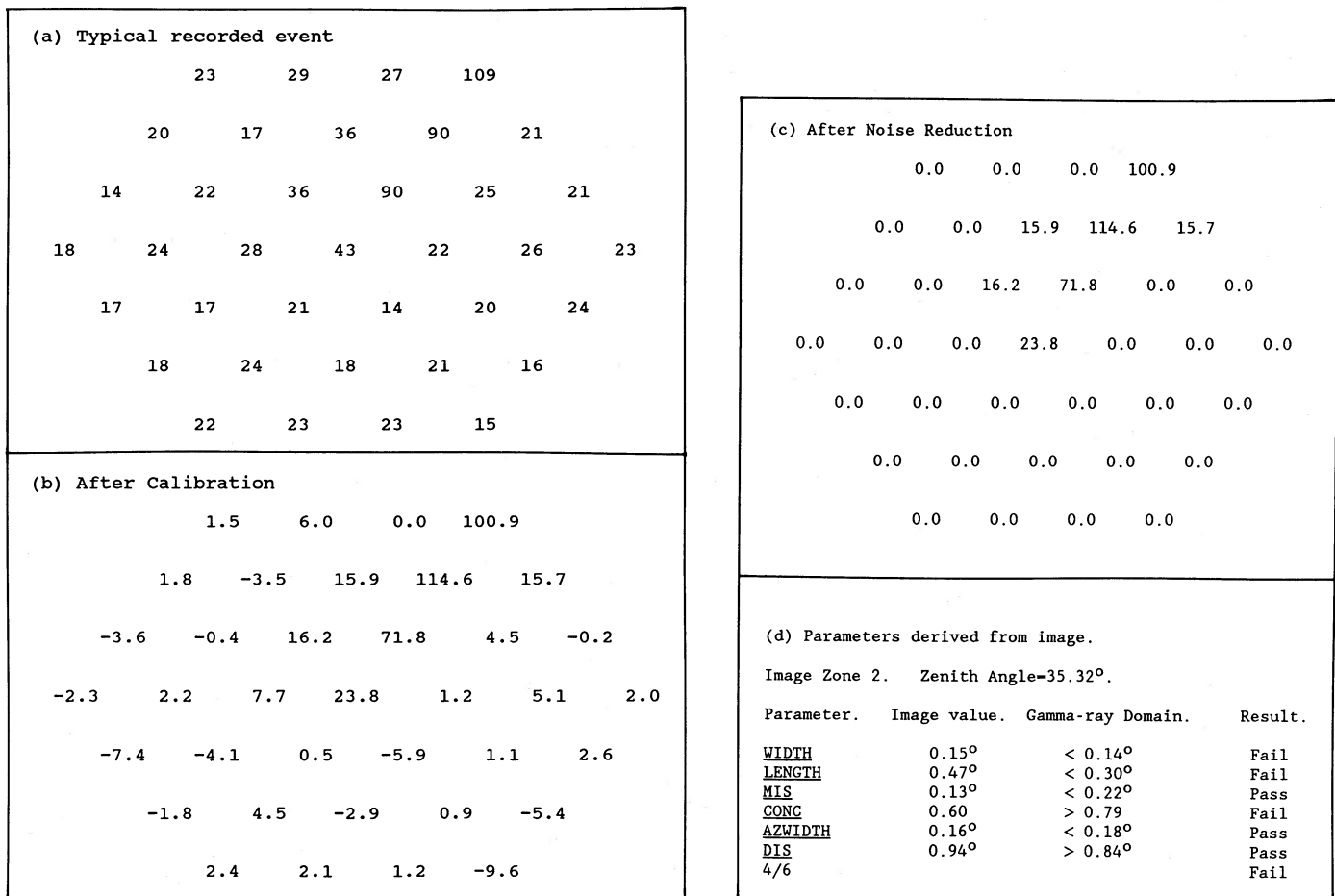
```
(a) Typical recorded event

            23       29       27      109

        20      17       36       90       21

     14     22       36       90       25       21

  18     24      28       43       22       26       23

     17      17       21       14       20       24

        18      24       18       21       16

            22      23       23       15

(b) After Calibration

            1.5      6.0      0.0    100.9

        1.8     -3.5     15.9    114.6     15.7

     -3.6     -0.4     16.2     71.8      4.5     -0.2

  -2.3     2.2      7.7     23.8      1.2      5.1      2.0

     -7.4     -4.1      0.5     -5.9      1.1      2.6

        -1.8      4.5     -2.9      0.9     -5.4

            2.4      2.1      1.2     -9.6
```

```
(c) After Noise Reduction

            0.0      0.0      0.0    100.9

        0.0      0.0     15.9    114.6     15.7

     0.0      0.0     16.2     71.8      0.0      0.0

  0.0      0.0      0.0     23.8      0.0      0.0      0.0

     0.0      0.0      0.0      0.0      0.0      0.0

        0.0      0.0      0.0      0.0      0.0

            0.0      0.0      0.0      0.0
```

(d) Parameters derived from image.

Image Zone 2.   Zenith Angle-35.32°.

Parameter.	Image value.	Gamma-ray Domain.	Result.
WIDTH	0.15°	< 0.14°	Fail
LENGTH	0.47°	< 0.30°	Fail
MIS	0.13°	< 0.22°	Pass
CONC	0.60	> 0.79	Fail
AZWIDTH	0.16°	< 0.18°	Pass
DIS	0.94°	> 0.84°	Pass
4/6			Fail

FIG. 2.—Typical image shown at various stages in the image processing: (*a*) raw image; (*b*) after pedestal subtraction and gain normalization; (*c*) after subtraction of subthreshold signal channels; (*d*) image parameters derived from (*c*), using the methods outlined in the appendix, and limits of gamma-ray domain.

i) *Normalization*

The first step in the calibration process was the subtraction of the pedestal values from each pixel in the image; in general, the pedestal levels were quite stable so that either the file recorded at the beginning or end of the night could be used for this purpose. The pedestals were preset to be ~ 20 digital counts.

The relative gain in the individual channels was determined in a two-step procedure: (*a*) the scan taken at the zenith and a random selection of scans taken through the night were used to normalize the pulse-height spectra of each channel in a given zone; (*b*) the relative gain between the zones was determined from the mean pulse heights of the nitrogen events. This two-stage process was necessary because of the differences in the spectral content of the nitrogen spark and the Cerenkov light pulse and the variation in the spectral sensitivity of the individual phototubes. In addition, triggering conditions and optical aberrations dictated that the response of the phototubes in each zone would differ slightly. The gains were set initially to be the same before calibration within $\pm 10\%$ (and were seldom more than $\pm 30\%$).

ii) *Editing Individual Images*

To minimize the effect of fluctuations in the piled-up night-sky (plus padding lamp) noise on measurements of a particular shower image, channels in which the pulse height was less than a preset threshold were set to zero. This threshold (10 digital counts = 14 photoelectrons) was approximately 3 times the observed rms value; this was determined from simulations to be the optimum threshold to use for this camera. Similarly, channels in which the recorded pulse height was less than 1% of the sum of the pulse heights in all channels were set to zero; this procedure minimizes the effect of small signals at a long distance from the image centroid. Again, this criterion was based on the analysis of computer-simulated images.

In this image preparation process a small number ($< 0.01\%$) of images were rejected in a filtering routine when it was obvious that the event was not caused by an air shower, e.g., electronic pickup, man-made light source, etc.

iii) *Philosophy*

Differentiation between gamma-ray shower images coming from a discrete source on the optic axis of the camera and from background hadronic showers coming from random directions rests on two distinct factors: (*a*) inherent differences in angular *size* and/or *shape* of the images from the two types of shower (gamma-ray and hadron); (*b*) differences between the image *orientation* based on the point of origin, i.e., on-axis discrete source or isotropic background. Basically the distribution of images from an on-axis source should appear to radiate from the center of the camera field of view, with the displacement of the image centroid and its "ellipticity" a function of the impact parameter between the shower axis and the detector axis. It is important to realize that these differences are independent and that their relative importance in differentiating the small gamma-ray signal from the cosmic-ray background will vary depending on the source spectrum, the camera threshold, the angular resolution, the trigger condition, etc. Ultimately the differentiation is limited by fluctuations in the development of the showers.

Although inherent differences in gamma-ray and proton shower images were predicted for the early image-intensifier cameras (Hill *et al.* 1963), the initial concept of the Whipple Observatory camera (Weekes 1981) was based on differentia-

tion via image orientation. In contrast, the atmospheric Cerenkov camera developed at the Crimean Astrophysical Observatory (Stepanian, Fomin, and Vladimirsky 1983) was designed to emphasize the differences predicted in the image types based on the early analytical shower calculations (Zatsepin 1965). Early Monte Carlo calculations differed in their prediction of the relative importance of these two methods of differentiation; simulations at Durham (Macrae and Turver 1982) indicated that the effect of fluctuations might mask the orientation differentiation, whereas independent simulations by Plyasheshnikov and Bignami (1985) found the orientation differentiation to be the major factor. More complete simulations at Leeds (Hillas 1985; Hillas and Patterson 1986; Hillas 1987) found that both approaches were important, and that the optimum discrimination was achieved using a combination of the two. This conclusion is verified by the results presented below.

iv) *Parameterization*

The relatively poor resolution of this camera and the high data rate did not justify sophisticated image analysis routines. Simple moment-fitting routines (see Appendix) were found to be most effective (MacKeown *et al.* 1983; Hillas 1985). To a first approximation the images are elliptical; if the major and minor axes are determined, then two parameters are easily defined: the *width* is a measure of the rms extent along the minor axis, and the *length* is a similar measure along the major axis. The extension of the major axis normally misses the center of the field of view (the source direction in the ON scans); the distance of closest approach (measured in degrees projected onto the sky) is called the *miss* parameter. Another useful parameter is distance, abbreviated as *dis*, which is defined as the distance between the centroid of the image and the center of the camera (Fig. 3).

An additional factor, concentration, abbreviated as *conc*, which was developed empirically, gave a simple measure of the concentration of the image; it was defined as the fraction of the light detected by the camera that is contained in the two brightest pixels. Originally known as *frac(2)*, it was used in the first imaging analysis of observations of the Crab Nebula (Cawley *et al.* 1985a).

A single parameter can be defined which combines the discrimination expected from size/shape and orientation criteria. This parameter, azimuthal width, abbreviated as *azwidth*, is the width measured perpendicular to the radius passing through the shower image centroid. This is really a combination of the discrimination achieved by *width* and *miss* and hence should be more effective than either acting alone.

v) *Image Selection*

Monte Carlo simulations of the response of the Whipple Observatory camera to both gamma-ray– and proton-initiated showers (using realistic values of the camera properties; Hillas 1985) predicted the distribution of shower parameters from a gamma-ray source on-axis relative to an isotropic background of cosmic rays. The detector is pointing to the zenith which is also the direction of the source. It was assumed that the gamma-ray source had a differential spectral index of -2.25 and the cosmic-ray background, one of -2.65. The results are shown in Figure 4. For ease of comparison, equal numbers of gamma rays and hadron shower image parameters are shown; in practice the gamma-ray signal will be only a small percentage of the background.
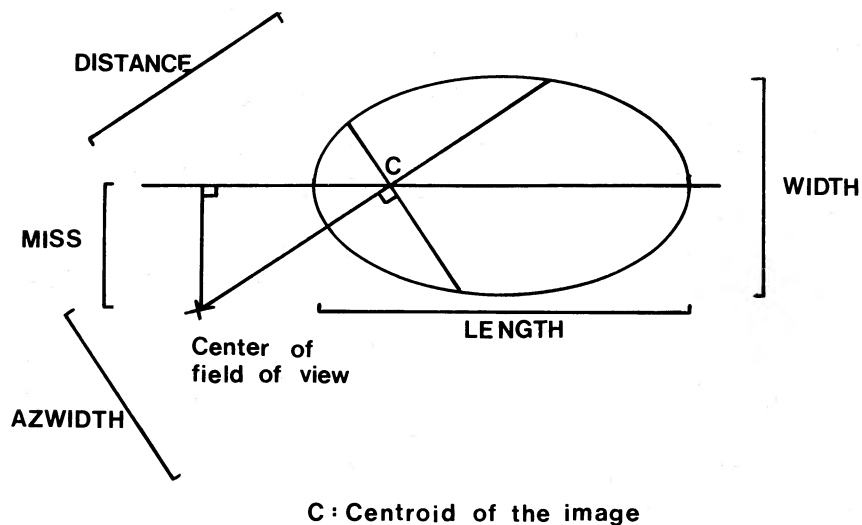
C : Centroid of the image

FIG. 3.—Definition of image parameters; also see Appendix
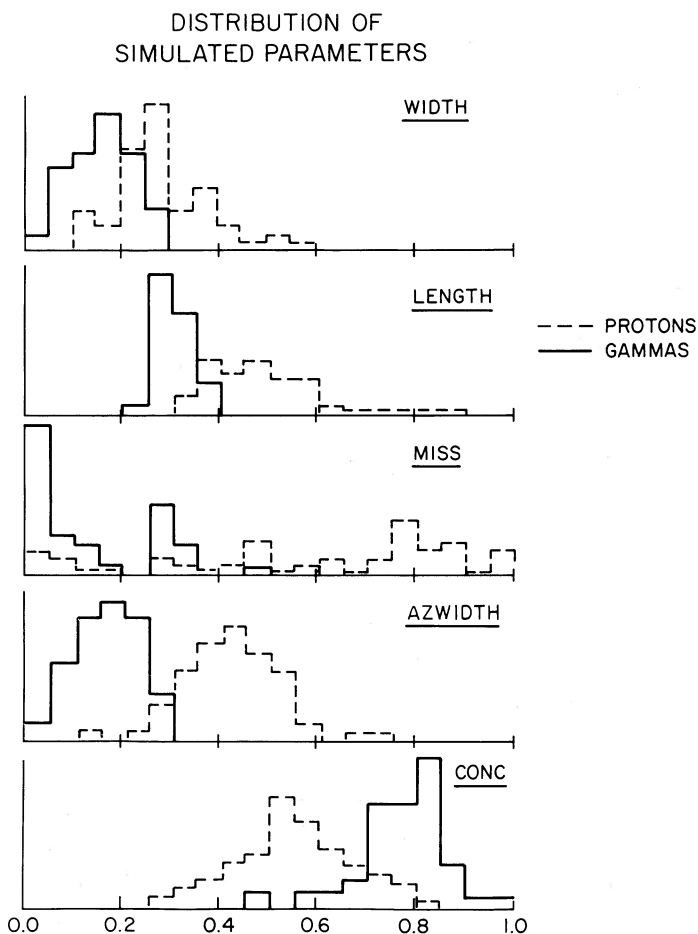
DISTRIBUTION OF
SIMULATED PARAMETERS

FIG. 4.—Image parameter distribution predicted by simulations for an on-axis gamma-ray source at the zenith and an isotropic background of cosmic rays. In all but *Conc* the scale is in degrees.

It is apparent that any one of these parameters could be used as an effective discriminator. In each case a gamma-ray domain is defined with a cutoff value which determines the range of parameter values where there is the maximum acceptance of gamma rays with the minimum contamination by background cosmic rays. These values, as determined from the simulations (Hillas 1985), are listed in Table 1; the images are classified by the zone in which the largest signal in the image occurs. As the zenith angle, z, increases, the ability of this camera to differentiate the gamma-ray showers from the hadronic background showers decreases because of the decreasing size of all shower images. The camera is expected to have its maximum sensitivity close to the zenith, although the exact response curve will be a function of the source energy spectrum.

Confidence in the ability of the simulations to predict the properties of the detected air shower images comes from a comparison of the measured parameters of the background cosmic-ray events with those predicted by the simulations. These are shown in Figure 5 for the various parameters; within the statistical limitations of the small number of simulations there is good agreement.

The precise definition of these domains is best achieved by experiment; however, this requires the detection of a strong gamma-ray signal. It is not unlikely that some relaxation of the cutoff values for the various parameters will increase the signal-to-noise ratio, since the simulations do not include such factors as the influence of pointing errors, the presence of sky-noise fluctuations, mirror misalignments, missing pixels, etc. Subsequent simulations have shown that none of these factors is serious and that they can be neglected initially. *Hence, for this analysis we have used the gamma-ray domain boundaries predicted by the simulations made prior to the observations; no optimization is involved, and no extra degrees of freedom must be accounted for in assessing the statistical significance of the result.*

The maximum discrimination is predicted by the simulations when either (*a*) the parameter domain boundaries are used in combination, e.g., when any four out of six of the particular image parameters are in the gamma-ray domain or (*b*) the parameter *azwidth* is used. We will report our results primarily in terms of *azwidth*. Simulations show this to be a

TABLE 1
PARAMETER CUTOFFS ($x = \sec z - 1$)

Parameter	Zone 1	Zone 2
Width .... (deg)	$< 0.21 - 0.17x$	$< 0.19 - 0.20x$
Length ...... (deg)	$< 0.35 - 0.13x$	$< 0.33 - 0.13x$
Miss .... (deg)	< 0.17	< 0.22
Dis .... (deg)	> 0.65	$> 0.83 + 0.04x$
Conc	$> 0.72 + 0.28x$	$> 0.72 + 0.31x$
Azwidth ..... (deg)	$< 0.21 - 0.11x$	$< 0.20 - 0.11x$

TABLE 2
OBSERVATION SUMMARY

Date	ON/OFF Pairs	Events ON	Events OFF	Difference
1986 Dec ...	21	97,306	97,782	−476
1987 Jan	32	123,292	122,917	+375
1987 Oct ...	10	34,534	34,689	−155
1987 Nov ...	52	182,790	182,308	+482
1987 Dec	12	46,191	45,847	+344
1988 Jan	16	59,643	59,471	+172
1988 Feb	32	109,218	108,787	+431
All	175	652,974	651,801	+1173

very effective discriminator since it is based on the two fundamental discrimination criteria (shape and orientation); also, it is easier to understand than a combination of only quasi-independent parameters. However, it is emphasized that the discrimination is found for all parameters (but with differing efficiency), as will be shown later.

III. RESULTS

a) Analysis

i) Data Base

The data base upon which the DC analysis is based is composed of 210 pairs of ON/OFF observations taken in the direc-
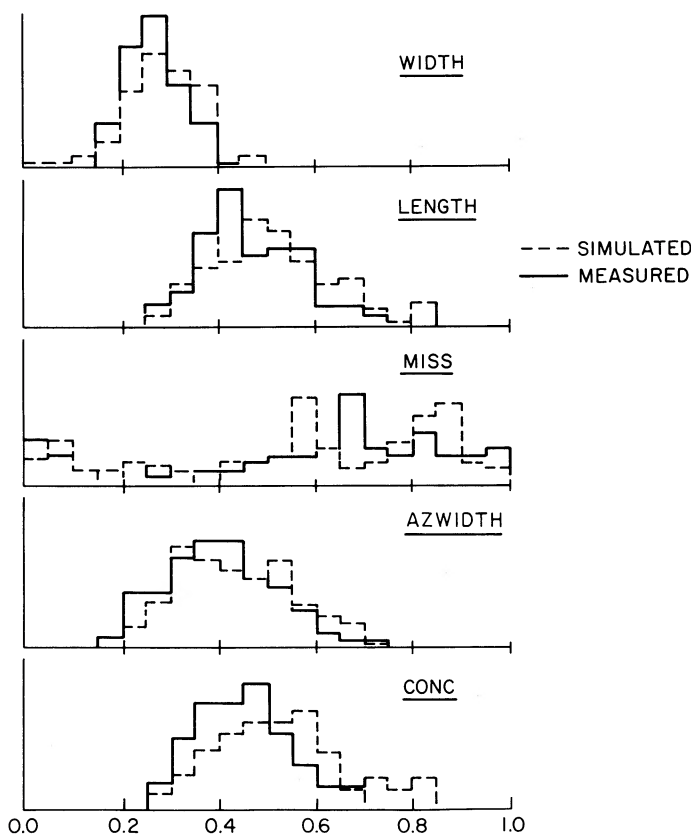
COMPARISON OF SIMULATED
AND MEASURED PARAMETERS

FIG. 5.—Comparison of predicted parameters of background cosmic rays with those actually measured by the camera. In all but Conc the scale is in degrees.

tion of the Crab Nebula (and control regions) between 1986 December and 1988 February. During this period the camera was also used to observe several other potential sources (Hercules X-1, Cygnus X-3, 4U 0115+63, the millisecond pulsars, etc.) often on the same night as the Crab observations. However, because of earlier indications of the success of this technique in detecting gamma rays from the Crab (Cawley et al. 1985a; Gibbs 1987), this source was given the highest priority when it was available for observation. The results of the analysis (without imaging selection) of the data from the observation of some of these other sources have been reported elsewhere (Gorham et al. 1985a, b; Cawley et al. 1985c; Cawley et al. 1987; Lamb et al. 1988).

The observation log, broken down by dark period, is shown in Table 2. No significant changes were made to the camera during this time, although the mirror surfaces steadily deteriorated (reflectivity decreasing from 90% to 70%) and were not recoated for the duration of the observations. A preliminary examination of the data base (but prior to any comparison of the ON/OFF raw data totals) led to the rejection of 35 ON/OFF pairs for various reasons, e.g., unequal lengths of scans, electronic problems, dramatic changes in minute-to-minute rates (suggesting weather changes), etc.

For the complete data base, the "all" data (no selection) totals show a +1173 excess on an OFF total of 651,801 showers in (175 × 28) minutes (+1.03 standard deviation [σ] using the statistics of Li and Ma 1985). The raw data totals broken down by image zone are shown in Table 3. The combined effect from images zones 0, 1, and 2 is +1.71 σ; only phototubes in these zones are involved in triggering the camera.

ii) Azwidth Selection

We have then applied the parameterization routines to each image and selected those falling within the gamma-ray domain. Using azwidth as discriminator, we obtained the results shown in Table 4. As suggested in Hillas (1985), only events with maximum light in zone 1 and 2 were considered in this analysis.

TABLE 3
CONTRIBUTION BY IMAGE ZONE

OBSERVATIONS	IMAGE ZONE			
	0	1	2	3
Events ON	32,758	197,120	280,498	142,598
Events OFF	32,661	196,859	279,130	143,151
Difference	+97	+261	+1,368	−553
Significance	+0.38	+0.42	+1.83	−1.03

TABLE 4

Azwidth DISCRIMINATION

Epoch	ON	OFF	All (%)	Difference	OFF (%)	Significance
			No Selection (All)			
1986–1988......	652,974	651,801	100.0	+1173	0.2	+1.03
			Azwidth Selection			
1986–1988......	9092	7929	1.2	+1163	14.7	+8.91

We note that (*a*) the percentage of events that are rejected by the *azwidth* discrimination threshold is greater than 98%, in agreement with the simulations (Hillas 1985); (*b*) there is an excess of candidate gamma-ray events in the ON source data of order 15%; (*c*) the effect is consistent with the difference in the "all" ON/OFF pairs, i.e., the selection has not rejected many gamma-ray events; (*d*) a significant excess is only seen when gamma-ray–like events are selected, so that there can be little doubt about the nature of the primary that causes the excess; (*e*) the cumulative total excess has a statistical significance of 8.9 σ; this is a level not generally encountered in very high energy or ultra high energy gamma-ray astronomy.

The overall distribution of *azwidth* parameters for the ON and OFF scans (for $z < 30°$) are shown in Figure 6. Also shown is the difference in detail for *azwidth* less than $0°.35$; this should be compared with Figures 4 and 5. Within the statistical limitations of the simulations (which were performed only for $z = 0°$), there is good qualitative agreement. We have also examined the differences in the two *azwidth* distributions over the full range for possible anomalies; these are plotted in Figure 7 as (ON − OFF) in standard deviations as a function of *azwidth*. It is apparent that the only significant differences are at small values of *azwidth*.

In Figure 8*a* we have plotted the distribution of individual (ON − OFF) effects (in standard deviations) in the 175 pairs using the *azwidth* canonical cut. To check on the run-to-run stability of the *azwidth* distributions we have also shown the distribution of (ON − OFF) effects using a cut at *azwidth* $> 0°.7$ (chosen to pass approximately the same number of events as the canonical cut passes at the other end of the distribution; i.e., ON = 15,163, OFF = 15,066, ON − OFF = 97 [+0.56 σ]). It is apparent that the distributions are within statistics apart from a net positive displacement in the canonical cut distribution. For comparison, we also show the same two distributions for 36 ON/OFF pairs of a control data set (discussed below) in Figure 8*b*.

ii) *Width and Miss Correlation*

Both the image shape and orientation discrimination contribute to the effect seen in *azwidth*, as is apparent in Table 5, in which the effect is also broken down by observing season.

iv) *Multiple Parameter Selection*

A net excess from the source direction is seen when discrimination is based on any one of the three parameters, *length*, *conc, or dis. Length* is a measure of the longitudinal develop-
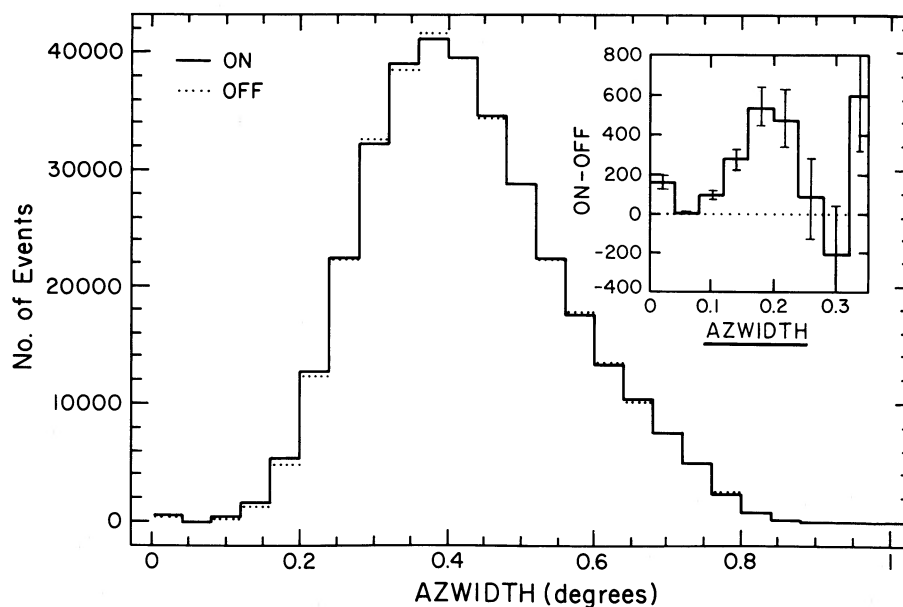

FIG. 6.—Distribution of "all" ON and OFF *azwidth* parameters (with $z < 30°$) for image zones 1 and 2 combined, with the differences in the two distributions in the gamma-ray domain shown in the inset.
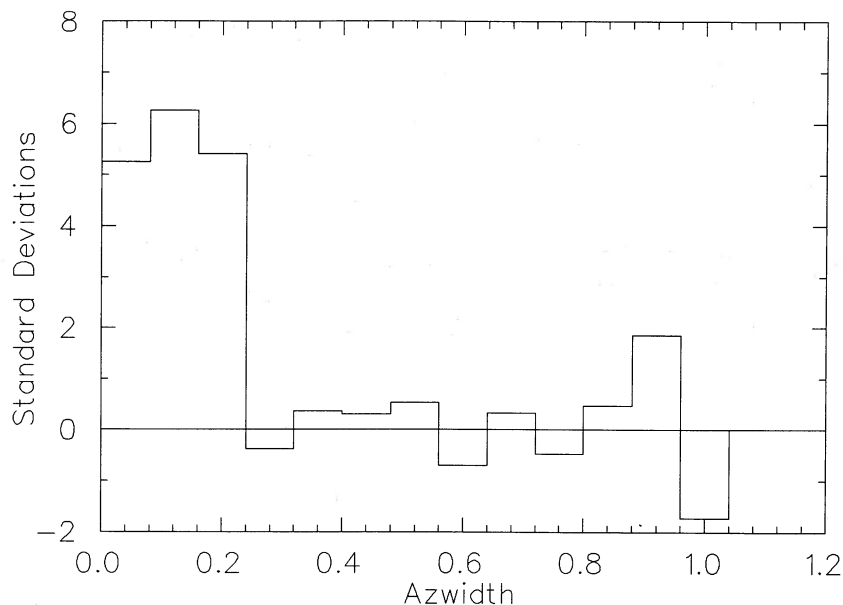
FIG. 7.—Distribution of *azwidth* (ON − OFF) in terms of standard deviations as a function of *azwidth*

ment of the shower and is hence quite different from *width* which is a strong function of the lateral spread. That it provides independent discrimination is an important confirmation of the photonic nature of the primary radiation. *Conc* is a combination of *width* and *length* and hence is not independent. *Dis* is the weakest discriminator in the simulations. This is seen to be the case here also (Table 6). When a combination of parameters is used, e.g., when four of the six parameter cuts are satisfied (as suggested by Hillas 1985), the effect is of comparable significance with the use of *azwidth* alone. An empirical selection (four out of five), with *dis* excluded, is even more significant ($+8.45\ \sigma$).

b) Previous Observations

In an early version of the camera (Clear *et al.* 1983; Cawley *et al.* 1985*b*), we made a series of observations of the Crab Nebula using basically the same technique. A total of 82 ON/OFF scans were made using the same observing technique as outlined above. Of these 40 were taken between 1983 November and 1984 January and 42 between 1984 October and 1985 March. Seventy of these were considered acceptable for

analysis. These observations were made prior to the detailed simulations with their prediction of distinct gamma-ray domains (Hillas 1985); however, an analysis based on an empirically defined parameter, *frac*(2) (now renamed *conc*), designed to exploit the difference between the measured angular size of Cerenkov light images and the simulated size of *gamma-ray* images, gave an excess of events from the direction of the Crab Nebula of 3–4 σ (Cawley *et al.* 1985*a*). An absolute significance could not be assigned to this excess since the separation into gamma-ray and background domains was empirically derived.

After the publication of the detailed simulations, this same data base was analyzed using the predicted discrimination factors (Gibbs 1987). The results are shown in Table 7. Although the statistical significance is not high, the results were sufficiently encouraging to warrant further observations using the upgraded camera.

Since there were significant differences between this data set and the 1986–1988 data set, we have chosen to treat them separately. In particular, (*a*) the camera trigger was different with the majority of the data taken with any one of the inner

TABLE 5

Azwidth, *Width*, AND *Miss* DISCRIMINATION

Epoch	ON	OFF	All (%)	Difference	OFF (%)	Significance
			Azwidth			
1986–1987......	2465	2231	1.01	+234	10.5	+3.41
1987–1988......	6627	5698	1.32	+929	16.3	+8.37
			Width			
1986–1987......	11,674	11,181	5.07	+493	4.4	+3.26
1987–1988......	31,453	30,417	7.06	+1036	3.4	+4.17
			Miss			
1986–1987......	30,220	29,905	13.55	+315	1.1	+1.28
1987–1988......	61,517	60,726	14.09	+791	1.3	+2.26

seven tubes triggered; (b) the camera electronics were custom built and subject to drifts not seen in the improved camera; (c) the influence of the star, Zeta Tau, was treated post facto in software, rather than in hardware as in the later observations.

Based on the excess seen with the *azwidth*, we estimate that the effect is compatible with a flux $1.47 \pm 0.28 \times 10^{-11}$ photons cm^{-2} s^{-1} with the gamma-ray energy threshold 0.6 TeV (Gibbs 1987). A factor of 1.5 uncertainty should be applied to both flux level and energy threshold.

c) Variation with Time

Previous observations of emission from the Crab Nebula had given some indication of variability, possibly associated with glitches in the pulsar period but with a 6 week delay (Fazio *et al.* 1972). To search for variability on a monthly time scale, the data has been analyzed by dark period. For *azwidth* as discriminator, the results are shown in Figure 9 and Table 8. We conclude that our measurements are consistent with a steady flux of gamma rays over the epoch 1986–1988. Within
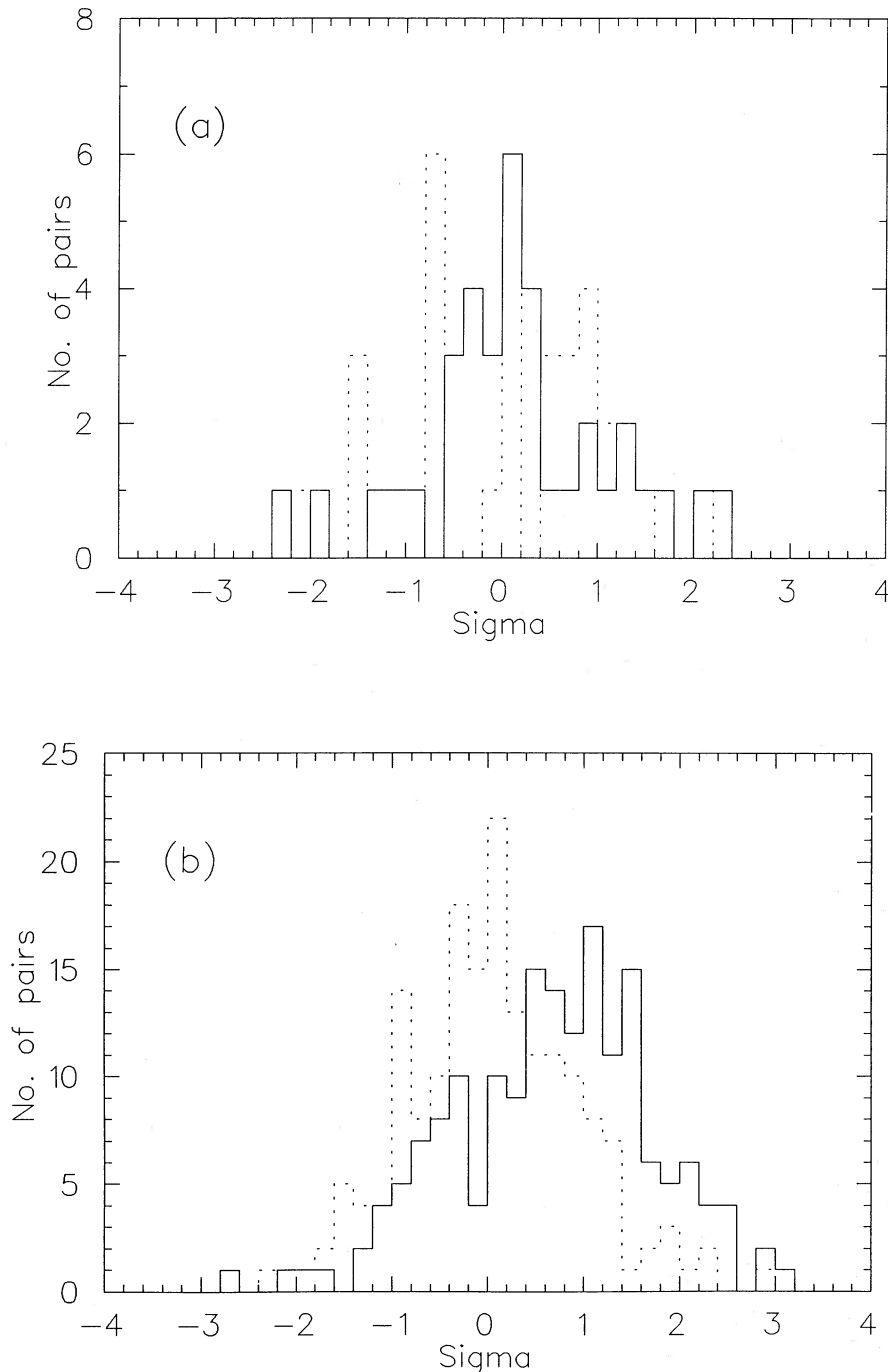

FIG. 8.—Difference in the *azwidth* ON and OFF values for cuts < 0°.21 (*solid line*) and > 0°.70 (*dotted line*) for (a) the 175 ON/OFF scans on the Crab Nebula and (b) the 36 ON/OFF scans on the control source.

TABLE 6

Length, Conc, Dis, AND MULTIPLE PARAMETER DISCRIMINATION

Parameter	ON	OFF	All (%)	Difference	OFF (%)	Significance
Length	25,868	24,931	3.82	+937	3.76	+4.16
Conc	15,222	14,206	2.18	+1016	7.15	+5.92
Dis	153,860	153,063	23.48	+797	0.52	+1.44
4/6	8256	7285	1.12	+971	13.33	+7.79

TABLE 7

RESULT SUMMARY 1983–1985

Parameter	ON	OFF	All (%)	Difference	OFF (%)	Significance
All	255,711	255,310	100.0	+401	0.16	+0.56
Azwidth	896	797	0.3	+99	12.42	+2.41
Width	3370	3277	1.3	+93	2.84	+1.14
Miss	56,853	56,189	22.0	+664	1.18	+1.97
4/6	630	504	0.2	+126	25.00	+3.74

the limitations of the earlier measurement (1983–1985), there is no evidence for variability over that larger time scale. As we shall see in the next section, the flux and energy derived are also consistent with the measurement made in 1969–1972. There was only one large glitch in the pulsar period (1986 August) between 1983 and 1988 (Lyne and Pritchard 1987); our observations did not begin until 1986 December, when we saw no increase in the observed flux. This is beyond the delay noted in the earlier observations. Thus the association of TeV gamma-ray emission with glitch activity is still problematic.

These results are the best evidence for the detection of a steady source of TeV gamma rays; this is in marked contrast to many of the recent reports of the detection of other sources where the emission is transient. This has significance not only

for the astrophysics of the nebula, but also for the future of the techniques in this energy range where progress has been severely hampered by the absence of a standard source (a so-called "standard candle"). Although this source is weak, in principle it can be used to compare and calibrate different telescopes.

d) Energy and Flux

Monte Carlo simulations of the response of this telescope to a gamma-ray source spectrum, which is a power law with differential exponent of −2.25, indicates an effective energy threshold of 0.5 TeV for zone 1 and 0.9 for zone 2. The values have been scaled by a factor of 1.25 from the values given in
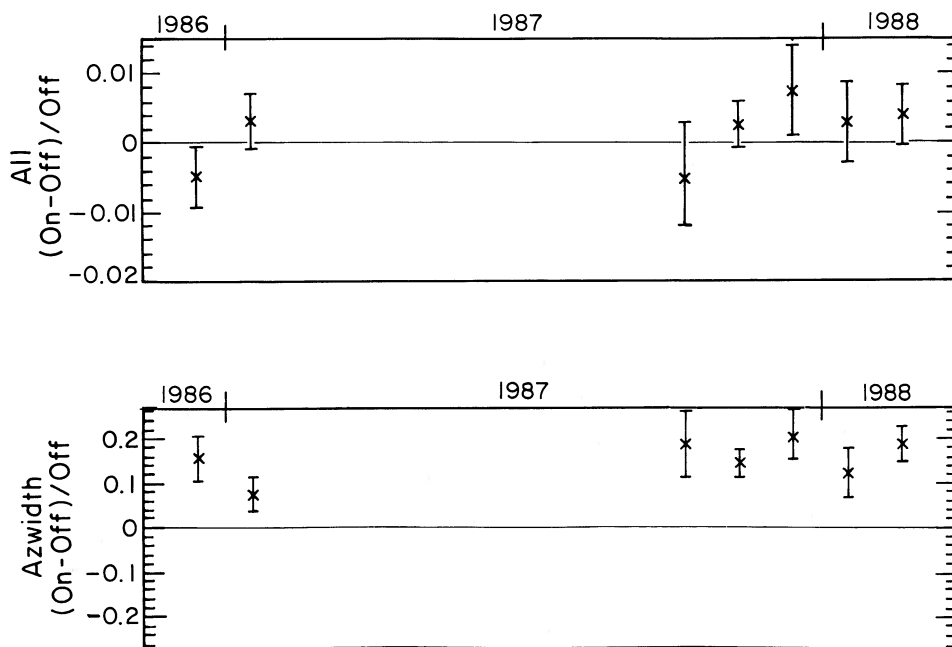

FIG. 9.—Variation with time (new moon) of the monthly (ON/OFF)/OFF values for unselected and *azwidth* selected data

WEEKES *ET AL.*

TABLE 8

MONTHLY VARIATION WITH *Azwidth*

Date	ON	OFF	All (%)	Difference	OFF (%)	Significance
1986 Dec	994	861	0.88	+133	15.45 ± 05.03	+3.09
1987 Jan	1471	1370	1.11	+101	7.37 ± 03.90	+1.89
1987 Oct	493	416	1.20	+77	18.51 ± 07.30	+2.55
1987 Nov	2785	2436	1.34	+349	14.33 ± 02.98	+4.83
1987 Dec	839	695	1.52	+144	20.72 ± 05.69	+3.68
1988 Jan	791	704	1.18	+87	12.36 ± 05.51	+2.25
1988 Feb	1719	1447	1.33	+272	18.80 ± 03.92	+4.83

Hillas (1985) in which an operating threshold of 40 p.e. was assumed (compared with the measured value of 50 p.e.).

The collection area and energy threshold vary with zenith angle; to derive a flux, we use the net excess observed with the *azwidth* discriminator for $z < 30°$ (574 events in zone 1 and 463 events in zone 2 in 116×28 minutes). Using the values given for collection area ($\pi \times [88 \text{ m}]^2$ for zone 1 and $\pi \times [117 \text{ m}]^2$ for zone 2), we derive a flux of 1.8×10^{-11} photons cm^{-2} s^{-1} for photons of energy greater 0.7 TeV. Further simulations are required to refine these values (whose systematic uncertainty is greater than the small formal statistical errors); we estimate an uncertainty of order of a factor of 1.5 in both values.

In principle, given the strength of the signal and the nature of the technique (in which the light can be integrated over the image and its impact parameter can be estimated from the image zone), it should be possible to derive an estimate of the shape of the emission spectrum. In practice, a full interpretation requires more detailed simulations of how the efficiency of gamma-ray event selection changes with energy. Some measure of the variation with energy can be seen from Table 9, in which the data (both "all" and *azwidth*-selected with zone 1 and 2 images combined) are divided into four brightness ranges according to the total integrated digital counts in each image. Note that the percentage of candidate gamma-ray events is a strong function of the brightness of the image. The brightest range (>3000 DC) is not significant, since it is dominated by events in which one or more pixels are saturated.

e) Consistency Checks

Since this is the first demonstration of the power of the imaging technique, we look for further evidence that the results are internally consistent with the detection of a flux of gamma rays. We have already shown that (i) apart from the differences in the gamma-ray domain, the ON and OFF distributions are similar; (ii) the net excess that is seen in *azwidth* is seen also in the two parameters that are the basis of this selection, *width and miss*, thus demonstrating that both shape and orientation are effective in selecting gamma rays; (iii) the excess is seen with the other parameter cuts also; in particular, we see the same strong effect when we use the four/six cut combination outlined by Hillas (1985); (iv) the excess is constant with time and evenly distributed over the 175 ON/OFF pairs; (v) there is evidence in an independent earlier data set for the same emission.

As further tests for possible systematic effects, we check the following: (vi) if the excess were noise-generated, it should be most apparent in the events that are just above threshold; division of the data by total digital counts recorded should show that the effect is not dominated by the least bright images; (vii) discrimination is less efficient at larger zenith angles; division of the data base by zenith angle should show that the technique is most sensitive close to the zenith; (viii) the effect of the star, Zeta Tau, should be shown to have no influence on the event selection; (ix) the order of observations (ON before OFF) should be shown to have no influence on the result.

vi) *Division by total intensity.*—The events which have the lowest total intensity do not show the net excess that would be expected if they were in some way triggered by an excess of noise, e.g., light fluctuations, in the vicinity of the Crab. We have already shown that subdivision of the data base into four broad ranges shows that the excess is distributed over two ranges that include more than two-thirds of the events (§ III*d* above). A further subdivision of the total data set to select only

TABLE 9

BREAKDOWN BY SHOWER BRIGHTNESS

ON	OFF	Difference	Significance	ON	OFF	Difference	Significance	RATIO
	ALL (no selection)				*Azwidth* (selected)			
				Total <300 DC				
163,057	161,813	+1244	+2.2	6719	5996	+723	+6.4	1.12
				300 DC $<$ Total $<$ 1000 DC				
339,693	339,937	−244	−0.3	1929	1535	+394	+6.7	1.26
				1000 DC $<$ Total $<$ 3000 DC				
119,924	119,523	+401	+0.8	401	370	+31	+1.1	1.08
				Total $>$ 3000 DC				
30,300	30,528	−228	−0.9	43	28	+15	+1.8	1.53

TABLE 10

DISTRIBUTION WITH ZENITH ANGLE (1986–1988)

Selection	ON	OFF	Difference	Significance
(a) $z < 30°$ (116 ON/OFF pairs)				
All	472,426	471,445	+981	+1.01
Azwidth	6708	5671	+1037	+9.32
(b) $z > 30°$ (59 ON/OFF pairs)				
All	180,548	180,356	+192	+0.32
Azwidth	2384	2258	+126	+1.85

images with brightness less than 200 DC ~15% of the total data base) shows that there is virtually no excess observed in this range that includes all events that are barely above threshold. In fact, the elimination of the bottom 15% of the events in the data set would enhance the significance of the excess seen using *azwidth* as discriminator.

vii) *Zenith angle.*—We have checked the efficiency of *azwidth* discrimination as a function of zenith angle by dividing the data base into those scans taken with the zenith angle predominantly (a) below 30°; (b) above 30°. The results are shown in Table 10; again they exhibit the expected behavior.

viii) *Effect of star.*—Although the presence of Zeta Tau is neutralized to the first order by the exclusion of the phototube in which it falls from the imaging process, there is a possible second-order effect on neighboring pixels. This point was checked through a series of observations taken under identical conditions on two control sources, carefully chosen so that in each case the "source" had a bright star (at least as bright as Zeta Tau) ~1° away from the center of the field of view. ON/OFF observations were taken in 1988 January and February, on the same nights on which the Crab was observed using the same operating mode. These observations constituted a control data set with almost identical night-sky background conditions as

the Crab observations. A total of 36 ON/OFF pairs were recorded with no significant excesses in any category of ON/OFF parameter selection. The distribution of (ON − OFF) effects with *azwidth* is shown in Figure 8b for the canonical cut and for *azwidth* $> 0°.7$.

ix) *Gain drift.*—In the early observations the usual pattern was to make ON observations and then the corresponding OFF observations. If the phototube or electronic gains changed in some fashion with time, i.e., with a change in temperature, this might give a systematic difference between the ON and OFF observations. In 1987–1988 we changed our operating procedure to check this possibility; 46 scans were made in which the normal order was reversed so that the OFF observations were made before the ON. It was apparent that the excess seen in the ON observations was independent of whether the control OFF scan was performed before or after the ON scan.

f) Periodicity Analysis

The angular resolution of the imaging technique (or any other technique at these energies) is not sufficient to distinguish emission coming from the Crab Nebula from that from the pulsar. The latter should be pulsed with the characteristic pulsar period and, therefore, can be distinguished from the steady unpulsed nebular emission.

Most of the observations of the Crab Nebula were taken by means of ON/OFF scans. In addition, tracking scans (ON without an accompanying OFF scan) were taken whenever sky conditions were not considered acceptable for the ON/OFF comparison. The data base for periodicity analysis consists of (a) all the ON runs used in the DC analysis (175 scans totaling ~82 hr); (b) tracking scans taken under nonoptimum weather conditions (39 scans totaling ~20 hr).

The arrival time of each shower was recorded with a resolution of 1 μs. The coordinated universal time (UTC) is maintained to an accuracy of ± 0.5 ms by a WWVB receiver. During the second season of observations (1987–1988), a
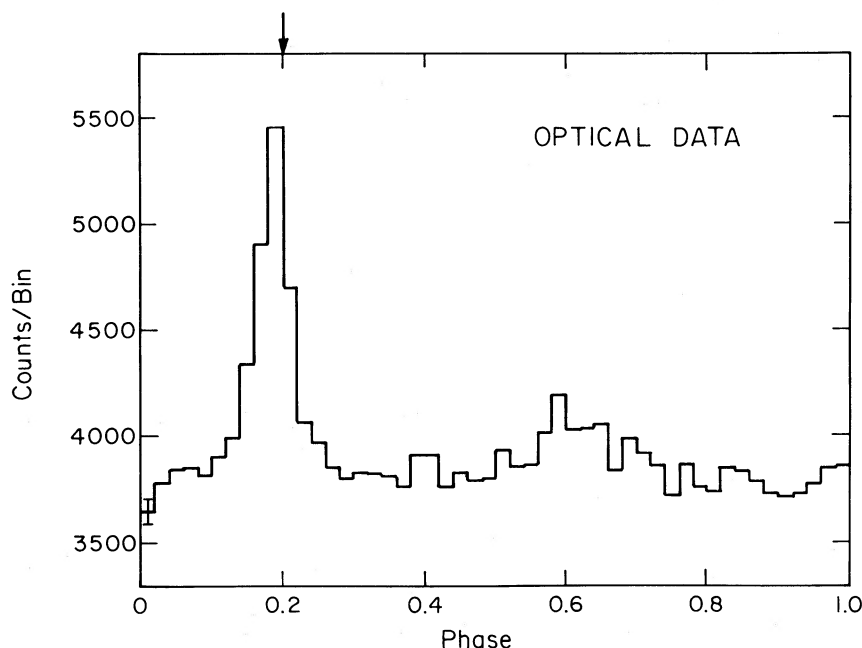

FIG. 10.—Light curve from optical observations of PSR 0531

Rubidium clock was added to the timing system. Absolute time was set on this portable clock relative to a time standard (caesium clock plus satellite receiver) at the nearby US Army Base of Fort Huachuca (Arizona) which maintained time to $< \pm 100$ μs. This intercomparison was performed at monthly intervals during the observing season. The arrival times in the observing frame were corrected for known clock drifts and then barycentered with the MIT (PEP311) ephemeris (Ash, Shapiro, and Smith 1967). Absolute phases were computed by folding the time series with the pulsar's radio ephemeris (Lyne and Pritchard 1988).

This is a very precise procedure, and it is essential that the timing system and analysis programs (barycentering, epoch folding, etc.) are accurate over the full span of observations. To check the correctness of each step, we undertook optical observations of PSR 0531+21 during 1987 December. A fast photometer was mounted at the focus of the 61 cm telescope on Mount Hopkins (located 100 m away from the 10 m reflector) and its output was fed through a coaxial cable to the gamma-ray camera electronics. Photon arrival times were recorded with the same procedure that was followed in the gamma-ray observations.

Figure 10 shows the light curve obtained by linking in phase six optical observations spread over 20 days (Vacanti *et al.* 1988). The arrow marks the position of the radio main peak. The agreement is good to one bin (~ 0.5 ms). Results from these optical observations give confidence in the correctness of our procedure as applied to the gamma-ray observations.

Periodicity analysis of the 10 m reflector data was in two steps. Initially all arrival times (no image discrimination to remove background) have been folded. Figure 11*a* shows the resultant light curve. No evidence for a periodic signal can be claimed. We estimate the pulsed component to be less than 0.35% of the cosmic-ray background (at the 2 σ confidence level for the pulsar emitting only during the main pulse—case 1 below).

In the second analysis, the parameter *azwidth* was used as before to reject more than 98% of the background events. The remaining 11,276 events were folded to give the light curve shown in Figure 11*b*. The arrow marks the position of the radio main pulse. There is a suggestion of a broad light curve, although not statistically significant (the most prominent bin stands 2.3 standard deviations over the average signal). Figure 9*c* shows the same set of data binned in 50 bins. Some suggestion of a pulsed emission still holds, but the latter is not concentrated in a narrow peak (as seen by Dowthwaite *et al.* 1984), and it is not coincident with the radio peak.

Making different assumptions on the extent of the phase interval during which the pulsar is emitting very high energy gamma rays, we compute a range of upper limits for the possible pulsed fraction. Taking as reference the 50 bin light curve (Fig. 11*c*), we define the following phase intervals as in the *COS B* results (Wills *et al.* 1982): main pulse (bins 9–13), intrapulse region (bins 14–27), interpulse region (bins 28–34), and background (bins 35–38).

Case 1.—The pulsar is ON for the main, intrapulse, and interpulse intervals. The OFF region is the background phase interval. There is an excess of 94 ± 100 events (0.9 σ), and a 2 σ upper limit to the pulsed fraction is estimated to be 0.25 of the net DC ON/OFF excess (less than 4.5×10^{-12} photons cm^{-2} s^{-1}).

Case 2.—The pulsar is ON for the main and interpulse; the background is estimated from the residual phase interval.
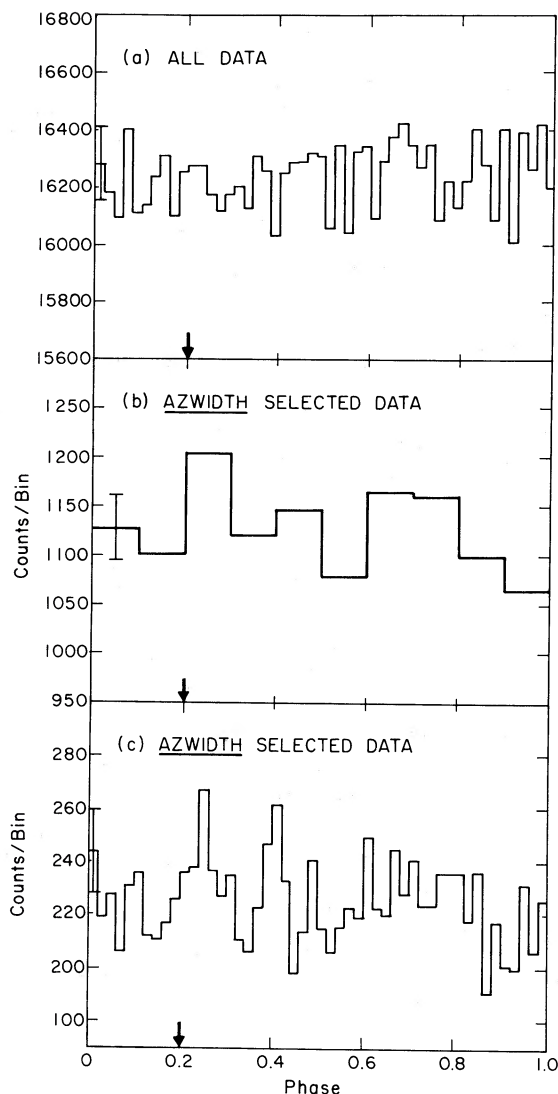

FIG. 11.—Light curves from air shower data: (*a*) unselected; (*b*) *Azwidth* selected, 10 bins; (*c*) *Azwidth* selected, 50 bins.

There is now an excess of 76 ± 54 events (1.6 σ), and the pulsed fraction is estimated at 0.06 ± 0.04 ($< 2.9 \times 10^{-12}$ photons cm^{-2} s^{-1}).

Case 3.—The pulsar is ON in the main pulse region only. The excess is now 42 ± 32 events (1.3 σ); the pulsed fraction is 0.04 ± 0.02 (less than 1.6×10^{-12} photons cm^{-2} s^{-1}).

We have also searched for evidence of episodic pulsed emission. A preliminary analysis shows no evidence for pulsed emission for intervals from tens of minutes to months.

Since the discovery of PSR 0531+21 several detections have been claimed for its TeV emission. Many light curve profiles have been reported, often at low confidence levels, which are not in agreement: they show one or two peaks; the main peak may be narrow (~ 1 ms; Dowthwaite *et al.* 1984) or broad (~ 6 ms; Tumer *et al.* 1985). Claims for burst activity on a time scale of minutes to months have been made as well (Gibson *et al.* 1982*b*; Bhat *et al.* 1986): again, there are conflicting claims for the widths of the detected peaks.

V. DISCUSSION

The detection of a flux of TeV gamma rays from the Crab Nebula is further evidence for the Compton synchrotron model of photon production within the system (Gould 1965). To date this extended gamma-ray spectrum has not been detected at other energies; given its steeply falling spectrum above 1 TeV, it is unlikely that the Crab Nebula will be detectable even with the new detectors planned for ultra high energy gamma-ray astronomy. At lower energies (100 MeV) a nonpulsed component has been detected, but its steep spectrum (Clear et al. 1987) is not compatible with a Compton synchrotron nebular origin; this could be an unpulsed component of the pulsar. The extrapolated flux (Fig. 12) falls a factor of 10 below the flux reported here.

Although there is always more than statistical uncertainty in the energy thresholds and collection areas assumed for air shower systems, there is at least qualitative agreement between the flux reported here and that reported by Fazio et al. (1972). Taken at their face value, these two measurements imply a flat spectrum (integral spectral index $= -0.7$); however, the earlier measurement should be reevaluated using the same Monte Carlo shower simulations used here (Hillas 1985). This new measurement is a confirmation of the value of the magnetic field derived from the earlier measurement (Grindlay 1976). This implies a uniform field close to the equipartition value of 6×10^{-4} G or a field that falls off radially from a value of 1×10^{-3} G at a radius of 0.1 pc from the pulsar. Although there was some suggestion of variability in the earlier data, both data sets are compatible with steady emission. The total flux of TeV gamma rays implied by these measurements that must be emitted by the Crab Nebula is greater than 1×10^{34} ergs s^{-1}. Only weak evidence is found for pulsed emission. This is clearly incompatible with the flux levels and light curves previously reported. However, there is little agreement between earlier reports where there is evidence for variability on time scales from minutes to months. Variability in the spectral shape of the emission at different phases of the Vela pulsar gamma-ray light curve has also been reported (Grenier, Hermsen, and Clear 1987). Clearly a deeper detection is required before any definitive conclusion can be reached.

The existence of a steady source of TeV gamma rays has important consequences for the development of the field. For years significant improvements have been hampered by the absence of a standard candle which would act as a means to calibrate and test new techniques. Although weak, the Crab Nebula appears to have the stability necessary for this role. It will be of interest therefore to compare the results from other experiments when they devote time to the study of the steady emission from this source.

The detection of the Crab Nebula at this level of statistical significance was only possible through the use of a technique which rejected more than 98% of the background events and which maintained careful controls of the ON and OFF observations. It is clear that major improvements in flux sensitivity can be made by systems which make detailed measurements of the Cerenkov light emission and exploit the differences between hadronic- and gamma-ray–initiated showers. Although the differences in the angular dimensions of the shower images were exploited here, similar improvements may result from other techniques that exploit other differences in the shower parameters. It is planned to test some of these techniques against imaging technique in the near future, using the gamma-ray flux from the Crab Nebula as a tagged beam.

If we are to exploit the imaging technique fully, it is clear that the optical resolution of the detector should be comparable or better than the scale of the gamma-ray shower images ($\sim 12'$). The angular resolution of the 10 m reflector ($15'$) is considerably better than the coarse pixel scale employed in this detector ($30'$); hence, the present camera is being replaced by one with pixel spacing of $15'$ (Lewis et al. 1987). It may also be
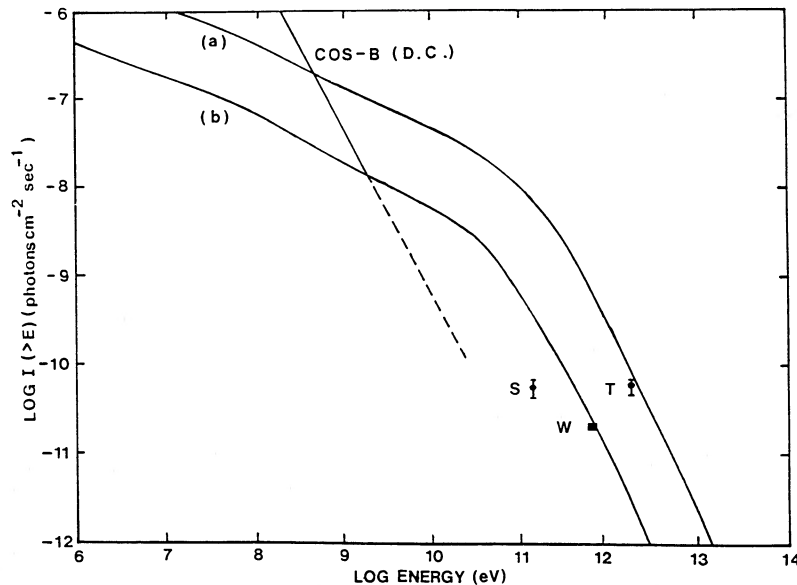

FIG. 12.—Compton-scattered spectrum of the Crab Nebula for two values of the magnetic field: (a) 10^{-4} G; (b) 3×10^{-4} G (Rieke and Weekes 1968). The extrapolated flux from the COS B measurements are shown as a dotted line (Clear et al. 1987). Measured points at TeV energies are S = Smithsonian (Fazio et al. 1972); T = Tien Shan (Mukanov 1983); W = Whipple (this work). Only the statistical errors are shown; there is a factor of 1.5 uncertainty in energy and flux in all three measurements.

advantageous to once again consider the use of image intensi-fier cameras with high resolution, coupled to optical telescopes (Mattox 1988). However, it has not yet been demonstrated that the same differentiation of gamma-ray–initiated air showers from the background can be achieved at higher energies.

A major advantage of the imaging technique is that it clearly differentiates the photon primary from the discrete source at the center of the field from the isotropic hadronic background. Hence the detection of a source immediately establishes that (*a*) the source is small (compared to the scale of the camera) and centered in the field; (*b*) the primaries detected are electromagnetic in nature and are most likely gamma rays.

APPENDIX

Suppose the ith phototube is given coordinates x_i, y_i (in degrees) and registers a signal s_i. The origin of the coordinates will be the center of the array of phototubes. The axis of an image is expressed by the equation:

$$y = ax + b .$$

Then defining (as usual)

$$\langle x \rangle = \Sigma_i s_i x_i/\Sigma_i s_i , \qquad \langle x^2 \rangle = E_i s_i x_i^2/\Sigma_i s_i , \qquad \langle y \rangle = \Sigma_i s_i y_i/\Sigma_i s_i ,$$

$$\langle y^2 \rangle = \Sigma_i s_i y_i^2/\Sigma_i s_i , \qquad \langle xy \rangle = \Sigma_i s_i y_i/\Sigma_i s_i ,$$

and

$$S_x^2 = \langle x^2 \rangle - \langle x \rangle^2 , \qquad S_y^2 = \langle y^2 \rangle - \langle y \rangle^2 , \qquad S_{xy} = \langle xy \rangle - \langle x \rangle \langle y \rangle .$$

If $d = S_y^2 - S_x^2$, then

$$a = \{d + \sqrt{[d^2 + 4(S_{xy})^2]}\}/2S_{xy} , \qquad b = \langle y \rangle - a\langle x \rangle ,$$

$$(width)^2 = (S_y^2 + a^2 S_x^2 - 2aS_{xy})/(1 + a^2) , \qquad (length)^2 = (S_x^2 + a^2 S_y^2 + 2aS_{xy})/(1 + a^2) ,$$

$$miss = ABS[(b)/\sqrt{(1 + a^2)}] , \qquad dis = r = \sqrt{(\langle x \rangle^2 + \langle y \rangle^2)} .$$

(NOT the shower impact parameter!).

To obtain the azimuthal width (*azwidth*), we first transform to coordinates (p, q) aligned along and perpendicular to the radial direction to the centroid. Then if

$$\sin \theta = \langle y \rangle/r \quad \text{and} \quad \cos \theta = \langle x \rangle/r ,$$

$$q = (\langle x \rangle - x) \sin \theta + (y - \langle y \rangle) \cos \theta .$$

Then *azwidth* is the rms spread in q:

$$(azwidth)^2 = \langle q^2 \rangle - \langle q \rangle^2 ,$$

the means being weighted by the signal in the phototube at coordinate (p, q), as in the original calculation of $\langle x \rangle$, etc.

REFERENCES

Ash, M. E., Shapiro, I. I., and Smith, W. B. 1967, *A.J.*, **72**, 338.
Bhat, P. N., Ramana Murthy, P. V., Sreekantan, B. V., and Vishwanath, P. R. 1986, *Nature*, **319**, 127.
———. 1987, *Proc. 20th Internat. Cosmic Ray Conf. (Moscow)*, **1**, 270.
Boone, J., Cady, R., Cassiday, G. L., Elbert, J. W., Loh, E. C., Sokolsky, P., Steck, D., and Wasserbaech, S. 1984, *Ap. J.*, **285**, 264.
Cawley, M. F., *et al.* 1985a, *Proc. 19th Internat. Cosmic Ray Conf. (La Jolla)*, (NASA CP-2376) **1**, 131.
———. 1985b, in *Proc. 19th Internat. Cosmic Ray Conf. (La Jolla)*, (NASA CP-2376) **3**, 453.
———. 1985c, *Ap. J.*, **296**, 185.
———. 1987, *Proc. 20th Internat. Cosmic Ray Conf. (Moscow)*, **1**, 240.
Clear, J., Bennett, K., Buccheri, R., Grenier, I. A., Hermsen, W., Mayer-Hasselwander, H. A., and Sacco, B. 1987, *Astr. Ap.*, **174**, 85.
Craig, M. A. B., Orford, K. J., Turver, K. E., and Weekes, T. C. 1981, *Proc. 17th Internat. Cosmic Ray Conf. (Paris)*, **1**, 3.
Davies, J. M., and Cotton, E. S. 1957, *J. Solar Energy, Sci. Eng.*, **1**, 16.
Dowthwaite, J. C., Harrison, A. B., Kirkman, I. W., Macrae, H. J., McComb, T. J. L., Orford, K. J., Turver, K. E., and Walmsley, M. 1984, *Ap. J. (Letters)*, **286**, L35.

Dzikowski, T., Gawin, J., Grochalska, B., and Wdowczyk, J. 1981, *Phil. Trans. Roy. Soc. London, A*, **301**, 641.
Erickson, R., Fickle, R., and Lamb, R. C. 1976, *Ap. J.*, **210**, 539.
Fazio, G. G., Helmken, H. F., O'Mongain, E., Rieke, G. H., and Weekes, T. C. 1972, *Ap. J. (Letters)*, **175**, L117.
Fegan, D. J., McBreen, B., O'Mongain, E., Porter, N. A., and Slevin, P. J. 1968, *Canadian J. Phys.*, **46**, S433.
Gibbs, K. 1987, Ph.D. thesis, University of Arizona.
Gibson, I. A., Harrison, A. B., Kirkman, I. W., Lotts, A. P., Macrae, J. H., Orford, K. J., Turver, K. E., and Walmsley, M. 1982a, *Nature*, **296**, 833.
———. 1982b, in *Proc. Workshop on Very High Energy Gamma-Ray Astronomy*, ed. P. V. Ramana Murthy and T. C. Weekes (Bombay: Tata Institute), p. 97.
Gorham, P. W. 1986, Ph.D. thesis, University of Hawaii.
Gorham, P. W., *et al.* 1986a, *Ap. J.*, **309**, 114.
———. 1986b, *Ap. J. (Letters)*, **308**, L11.
Gould, R. J. 1965, *Phys. Rev. Letters*, **15**, 511.
Grenier, I. A., Hermsen, W., and Clear, J. 1987, *Proc. 20th Internat. Cosmic Ray Conf. (Moscow)*, **1**, 77.
Grindlay, J. E. 1971, *Smithsonian Ap. Obs. Spec. Rept.*, No. 334.

Grindlay, J. E. 1972, *Ap. J.* (*Letters*), **174**, L9.
———. 1976, in *Proc. Gamma-Ray Symposium*, ed. C. E. Fichtel and F. W. Stecker (Greenbelt, MD: Goddard Space Flight Center), p. 84.
Grindlay, J. E., Helmken, H. F., and Weekes, T. C. 1976, *Ap. J.*, **209**, 592.
Grindlay, J. E., and Hoffman, J. A. 1971, *Ap. Letters*, **8**, L209.
Gupta, S. K., Ramana Murthy, P. V., Sreekantan, B. V., and Tonwar, S. C. 1977, in *Proc. 15th Internat. Cosmic Ray Conf.* (*Plovdiv*), **1**, 114.
Helmken, H. F., Fazio, G. G., O'Mongain, E., and Weekes, T. C. 1973, *Ap. J.*, **184**, 245.
Hermsen, W., *et al.* (Caravane collaboration). 1977, in *Proc. 12th Eslab Symposium*, ed. R. D. Wills and B. Battrick (ESA SP-124), p. 13.
Hill, D. A., Overbeck, J., White, J., Long, C. D., Porter, N. A., Jelley, J. V., and Fruin, J. 1963, *Proc. Inter-American Cosmic Ray Conf.*, **46**, 1.
Hill, D. A., and Porter, N. A. 1961, *Nature*, **191**, 690.
Hillas, A. M. 1985, *Proc. 19th Internat. Cosmic Ray Conf.* (*La Jolla*), **3**, 445.
———. 1987, *Proc. Italian Phys. Soc.*, **8**, 325.
Hillas, A. M., and Patterson, J. R. 1986, in *Proc. NATO Adv. Workshop on Very High Energy Gamma-Ray Astronomy*, ed. K. E. Turver (Dordrecht: Reidel) p. 243.
Jennings, D. M., White, G., Porter, N. A., O'Mongain, E., Fegan, D. J., and White, J. 1974, *Nuovo Cimento*, **20**, 71.
Kirov, I. N., *et al.* 1985, *Proc. 19th Internat. Cosmic Ray Conf.* (*La Jolla*), **1**, 135.
Kniffen, D. A., Fichtel, C. E., Hartman, R. C., Lamb, R. C., and Thompson, D. J. 1977, in *Proc. 12th Eslab Symposium*, ed. R. D. Wills and B. Battrick (ESA SP-124), p. 45.
Lamb, R. C., *et al.* 1988, *Ap. J.* (*Letters*), **328**, L13.
Lewis, D. A., *et al.* 1987, *Proc. 20th Internat. Cosmic Ray Conf.* (*Moscow*), **2**, 338.
Li, T., and Ma, Y. 1985, *Ap. J.*, **272**, 317.
Lyne, A. G., and Pritchard, R. S. 1987, *M.N.R.A.S.*, **229**, 223.
———. 1988, private communication.
MacKeown, P. K., Cawley, M. F., Clear, J., Fegan, D. J., Lamb, R. C., Turver, K. E., and Weekes, T. C. 1983, *Proc. 18th Internat. Cosmic Ray Conf.* (*Bangalore*), **9**, 175.
Macrae, J. H., and Turver, K. E. 1982, private communication.

Mattox, J. 1988, private communication.
Mukanov, J. B. 1983, *Izv. Krimsk. Astrofiz. Obs.*, **67**, 55.
Plyasheshnikov, A. V., and Bignami, G. F. 1985, *Nuovo Cimento*, **8C**, 39.
Porter, N. A., Delaney, T., Helmken, H. F., and Weekes, T. C. 1976, *Nuovo Cimento*, **32B**, 514.
Porter, N. A., and Weekes, T. C. 1978, *Smithsonian Ap. Obs. Spec. Rept.*, No. 381.
Resvanis, L., *et al.* 1986, in *Proc. NATO Advanced Workshop on Very High Energy Gamma-Ray Astronomy*, ed. K. E. Turver, (Dordrecht: Reidel), p. 225.
Rieke, G. H. 1969, *Smithsonian Ap. Obs. Spec. Rept.*, No. 301.
Rieke, G. H., and Weekes, T. C. 1969, *Ap. J.*, **15**, 577.
Stepanian, A. A., Fomin, V. P., and Vladimirsky, B. M. 1983, *Izv. Crimean Astrofiz. Obs.*, **66**, 234.
Tumer, O. T., Wheaton, W. A., Godfrey, C. P., and Lamb, R. C. 1985, *Proc. 19th Internat. Cosmic Ray Conf.* (*La Jolla*), (NASA CP-2376) **1**, 139.
Vacanti, G., *et al.* 1988, in *Proc. NATO Workshop on Cosmic Gamma Rays and Neutrinos*, ed. M. M. Shapiro and J. Wefel (Dordrecht: Reidel), in press.
Vishwanath, P. R. 1982, in *Proc. Internat. Workshop on Very High Energy Astronomy*, ed. P. V. Ramana Murthy and T. C. Weekes (Bombay: Tata Institute), p. 21.
———. 1986, in *Proc. NATO Workshop on Very High Energy Gamma-Ray Astronomy*, ed. K. E. Turver (Dordrecht: Reidel), p. 147.
———. *et al.* 1985, *Proc. 19th Internat. Cosmic Ray Conf.* (*La Jolla*), (NASA CP-2376) **1**, 144.
Watson, A. A. 1985, *Proc. 19th Internat. Cosmic Ray Conf.* (*La Jolla*), NASA CP-2376) **9**, 111.
Weekes, T. C. 1981, *Proc. 17th Internat. Cosmic Ray Conf.* (*Paris*), **8**, 34.
Weekes, T. C., and Turver, K. E. 1977, in *Proc. 12th Eslab Symposium*, ed. R. D. Wills and B. Battrick (ESA SP-124), p. 279.
Wills, R. D., *et al.* 1982, *Nature*, **296**, 723.
Zatsepin, V. I. 1965, *Soviet Phys. JETP*, **20**, 459.
Zyskin, Y. L., Vladimirsky, B. M., Neshpor, Y. I., Stepanian, A. A., Fomin, V. P., and Shitov, V. G. 1987, *Proc. 20th Internat. Cosmic Ray Conf.* (*Moscow*), **2**, 342.

M. F. CAWLEY: Physics Department, St. Patrick's College, Maynooth, County Kildare, Ireland

D. J. FEGAN, N. A. PORTER, and P. T. REYNOLDS: Physics Department, University College, Belfield, Dublin 4, Ireland

K. G. GIBBS: Enrico Fermi Institute, University of Chicago, 5640 South Ellis Avenue, Chicago, IL   60637

A. M. HILLAS: Department of Physics, University of Leeds, Leeds, LS2 9JT, England, UK

P. W. KWOK, G. VACANTI, and T. C. WEEKES: Whipple Observatory, Box 97, Amado, AZ   85645-0097

R. C. LAMB, D. A. LEWIS, and D. MACOMB: Physics Department, Iowa State University, Ames IA   50011